



# Computational modeling of coupled mechanical damage and electrochemistry in ternary oxide composite electrodes

Jiaxiu Han, Nikhil Sharma, Kejie Zhao\*

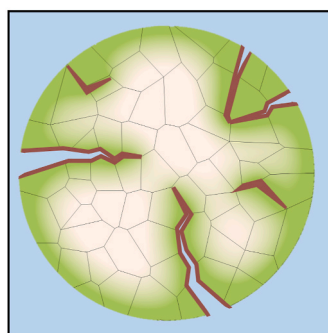
School of Mechanical Engineering, Purdue University, West Lafayette, IN 47906, USA

## HIGHLIGHTS

- A coupled electro-chemo-damage computational framework.
- Mechanical damage due to intergranular fracture of NMC cathode particles.
- Electrolyte infiltration along the damaged polycrystalline grain boundaries.
- Corrosion and impeded interfacial charge transfer at the fractured surfaces.
- Increased capacity but aggravated mechanical damage due to electrolyte infiltration.

## GRAPHICAL ABSTRACT

### Damage-electrochemistry coupling



■ Electrolyte ■ Li ■ Damage

## ARTICLE INFO

### Keywords:

Ternary oxide  
Composite cathode  
Fracture  
Battery degradation  
Modeling

## ABSTRACT

Performance degradation of ternary layered oxide cathodes largely originates from their loss of structural integrity in cyclic usage. Mechanical damage, such as intergranular fracture of the active particles, is not only a mechanical cleavage process but also interferes with electrochemical kinetics such as infiltration of liquid electrolyte, surface corrosion of the constituent primary particles, and may eventually isolate the primary grains from the electron conducting network. Here we develop a computational framework that integrates electrochemistry of a  $\text{LiNi}_x\text{Mn}_y\text{Co}_{1-x-y}\text{O}_2$  (NMC) composite cathode with mechanical damage of the active particles. To fully examine the intricate chemomechanical behavior of the electrode, we evaluate the effects of the anisotropic material properties, the influence of mechanical potential on Li transport, and the concurrent intergranular fracture and electrolyte penetration along the grain boundaries upon multiple cycles. Electrolyte infiltration benefits capacity retention but aggravates further mechanical damage by corrosion. Structural failure mostly occurs in the first charging due to the anisotropic mechanical strain between the primary grains, while the resulting damage remains stable in the later few cycles. The results are consistent with experimental observations and the integration of electrochemistry and mechanical failure enables a step further understanding of the complex mechanism of battery degradation.

\* Corresponding author.

E-mail address: [kjzhao@purdue.edu](mailto:kjzhao@purdue.edu) (K. Zhao).

<https://doi.org/10.1016/j.jpowsour.2023.234034>

Received 26 July 2023; Received in revised form 24 December 2023; Accepted 29 December 2023

Available online 14 January 2024

0378-7753/© 2024 Elsevier B.V. All rights reserved.

## 1. Introduction

Along the pathway toward net zero emission [1], the energy storage solution must meet the increasingly demanding requirements of high energy density, fast charging, long cycle life, and low cost. Li-ion batteries have emerged as one of the most commercially successful energy storage devices, especially in portable electronics and electric vehicles [2]. Among the various cathode materials used in Li-ion batteries, ternary layered oxide  $\text{LiNi}_x\text{Mn}_y\text{Co}_{1-x-y}\text{O}_2$  represents the state-of-the-art which offers a balanced merit between energy density, power density, and stability [3]. By increasing the nickel content in NMC, its discharge capacity, voltage, and energy density can be further enhanced, but the drawback comes with severe structural degradation [4,5]. Understanding the mechanical activation and mitigating the resulted degradation therefore become crucial in achieving the optimal performance of NMC cathodes.

The mechanical behavior of NMC is largely determined by its anisotropic material properties. Due to the layered lattice structure, NMC exhibits several intrinsic anisotropic features including anisotropic Li diffusivity [6], anisotropic mechanical properties [7], and anisotropic chemical strains upon redox reactions [8]. Commercial NMC particles adopt a hierarchical morphology to achieve a higher tap density, where small primary particles aggregate to form spherical polycrystalline secondary particles [9]. Within the polycrystalline structure, the anisotropic diffusivity along the *c*-axis versus *ab*-plane creates a tortuous Li pathway, leading to charge heterogeneity and non-uniform distribution of chemical strains that generate stresses [6]. We used nano-indentation to measure the anisotropic stiffness matrix of NMC [7]. Various diffraction experiments have been conducted to determine the anisotropic chemical strains (variation of lattice changes in the *a*- and *c*-axes during (de)lithiation) [8,10,11]. The anisotropic chemical strains within the randomly orientated primary particles cause significant mismatched deformation and stresses along the boundaries between neighboring primary grains. Overall, charge heterogeneity and anisotropic lattice strains lead to intergranular fracture and disintegration of the NMC secondary particles.

The mechanical behavior of electrodes is also intimately coupled with the thermodynamics and dynamics of electrochemistry. Mechanical stresses can regulate the kinetics such as Li diffusion and interfacial charge transfer [12,13], and influence electrochemical behaviors within the single particles, between neighboring particles, and among the electrode composite [14,15]. Besides, high-capacity electrode materials such as NMC cathode and Si anode exhibit a broad range of Li concentrations that vastly deviate from the ideal dilute solution. Therefore, the solution nonideality due to the interactions of the guest species must be considered in the Cahn chemical potential [16,17], which has been proved to place a significant effect on Li diffusion and the electrochemistry response in Si electrodes [13,18]. One of the goals of this work is to assess the mechanical effect on Li transport in NMC cathode by considering the anisotropic transport and mechanical properties and the thermodynamic nonideality of the solid solution electrode.

Moving forward, our major goal is to integrate the modeling of electrochemical performance and mechanical damage of a composite electrode and evaluate their mutual interactions upon cycling. Intergranular fracture of polycrystalline NMC particles is the primary cause of structural disintegration in Ni-rich cathodes [11,19]. Cracks break the cohesion between primary particles and distort the Li transport channels, thereby deteriorating the rate performance. Severe fractures eventually isolate primary particles from the electron conductive matrix, rendering them “dead particles” that lead to the loss of capacity [20]. There has been extensive research on mechanical damage through numerical modeling. Prior work has studied the effects of charging rate, fracture energy, particle size and morphology, cycling protocol, and anisotropy on electrochemical performance and damage behaviors [21–24] and simulated damage by utilizing the cohesive zone method, spring model, and phase-field modeling [25]. Despite the considerable

literature on computational modeling of the fracture behavior of NMC particles, the coupling between damage generation and electrochemical kinetics is not fully explored – for instance, the freshly fractured surface welcomes electrolyte infiltration, which can result into parasitic surface reactions, such as phase transformation [26], oxygen release [27], transition metals dissolution [28], and corrosion of the intergranular strength [29]. Electrolyte infiltration has been observed in many experiments and considered in theories. Xia et al. found that electrolyte penetration shortens Li diffusion pathway but not for electron conduction, inducing a mismatched transport of charge carriers [30]. Janek et al. studied the effect of cracks and electrolyte infiltration on Li transport in both liquid and solid electrolyte environments [31]. They observed faster Li diffusion and higher capacity over cycles using a liquid electrolyte compared to the solid case. Min et al. recently proposed that electrolyte penetration and the incurred electrochemical reaction inside the NMC particles are responsible for the observation that Li diffusion time is independent of the secondary particle size [32]. In a prior work, we demonstrated positive feedback between surface charge heterogeneity and bulk fracture by considering electrolyte infiltration as a fast channel of Li transport [33]. Nevertheless, it remains a challenging task to incorporate electrolyte infiltration and its effects on electrochemical response and mechanical damage in the composite electrode.

Herein, we first examine the effect of various anisotropic features of NMC including anisotropic Li diffusivity, anisotropic mechanical properties, and anisotropic chemical strains. Anisotropy is the key to capture the charge heterogeneity and enormous stresses at the grain boundaries in the polycrystalline particles. Next, we quantitatively evaluate the mechanical effect on Li diffusion and voltage response in the NMC composite cathode. We show that solution nonideality is the primary factor regulating the diffusion kinetics. While mechanical potential is non-trivial at slow and moderate charging rates, at a fast-charging rate, the mechanical effect becomes negligible. Lastly, we conduct finite element analysis based on a fully coupled electrochemistry-fracture model to study the consequence of damage generation and electrolyte infiltration on Li transport, damage evolution, and capacity retention. The electrolyte wetting reduces the intergranular fracture strength of the polycrystalline NMC, while simultaneously improving Li diffusion kinetics and capacity retention by increasing the surface area where charge transfer reactions are upon. We also observe that most of mechanical damage emerges in the first charging process and then the electrochemical response and mechanical damage of the cathode become stable over the next few cycles in both the solid-state and liquid-electrolyte batteries. The computational framework integrating the electrochemical kinetics and mechanical failure provides further insight into the complex mechanism of battery degradation.

## 2. Theories and computational model

A Li-ion battery is composed of three main components, a positive electrode (cathode), a negative electrode (anode), and an electrolyte wetting both electrodes, as shown in Fig. 1(a). Li ions migrate from the cathode to the anode through the electrolyte during charging, and electrons transport through the external circuit. The charge transfer reaction  $\text{Li}^+ + e^- \rightarrow \text{Li}$  takes place at the interface between the anode and the electrolyte to deposit lithium. In the cathode, NMC particles mix with carbon and polymeric binders to form a porous composite soaked with the liquid electrolyte. As shown in Fig. 1(a), the NMC particle is represented by the beige circle of multiple random shaped polygons. The liquid electrolyte, represented by the light blue domain in Fig. 1(a), provides the diffusion channel for Li ions between the cathode and the anode. The porous carbon-binder matrix, represented by the grey domain, forms the conductive network for electrons and physical support for the active particles. We build a half-cell model to simulate the co-evolving electrochemical and mechanical behaviors during the charging and discharging cycles. There are five electrochemical processes to be considered, including (I) Li diffusion within the active

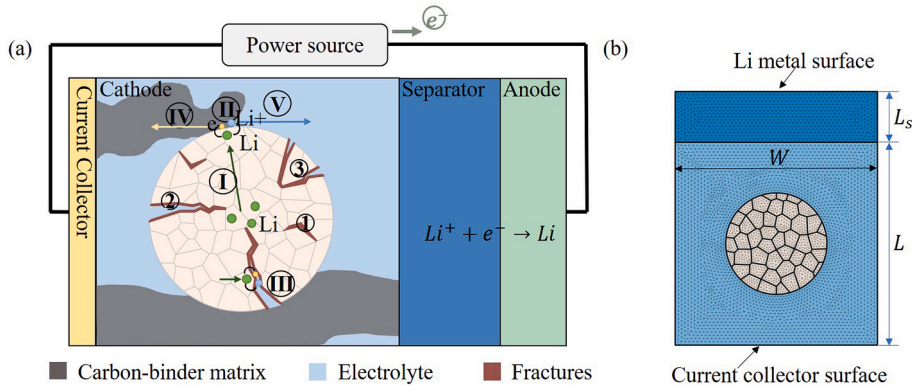
materials, (II) interfacial charge transfer at the NMC outer surfaces, (III) interfacial charge transfer at the fractured surfaces (considering electrolyte infiltration), (IV) electron conduction in the carbon-binder matrix, and (V) Li ions diffusion in the electrolyte. For (I), we also evaluate the mechanical effect on Li diffusion and voltage response. During cycling process, (de)lithiation-induced strains generate mechanical stresses, resulting in intergranular fracture of NMC particles. Depending on the severity, mechanical damage may be considered as (1) minor cracks, (2) major cracks, or (3) complete cracks that isolate the primary grains. Minor cracks are small-sized cracks that do not further grow, while the major cracks are formed by propagation of small-sized ones and association with other minor cracks, reaching the particle surface and introducing electrolyte infiltration into the interior particles. Isolated particles are formed by complete cracks, which block electrons conduction, thus becoming inactive particles. We apply a fully coupled electro-chemo-mechanics theory, which describes the kinetics of Li ions transport and electron conduction in the battery cell, deformation kinematics and stresses of the composite cathode, dynamics of crack growth of the active particles, the mechanical effect on Li diffusion, and the effects of evolving fracture on the interfacial charge transfer reaction.

Fig. 1(b) shows the geometry of the half cell and mesh in the finite element modeling, which includes a current collector, a NMC polycrystalline active particle, an electrolyte-carbon-binder domain, a separator, and a Li metal anode. In this model, the mechanical interaction between the active particle and the conductive matrix is not considered. Therefore, for the computational simplicity, a continuum electrolyte-carbon-binder domain has been applied, which is different from the explicit configurations of the electrolyte and carbon-binder outlined in Fig. 1(a). The radius of the active particle is set as  $5 \mu\text{m}$ . The polygonal primary particles are generated of random shapes and sizes using the Voronoi tessellation [34], which have an average diameter around  $1.5 \mu\text{m}$ . Such a size is slightly larger than the primary particles in experiments [35] but it affords a reasonable balance between the computational cost and accuracy. The thickness of the Li metal anode and current collector is set as zero to focus on the response on the cathode side.  $L$  represents the height of the porous cathode,  $L_s$  the height of the separator, and  $W$  the width of the porous cathode. All the modeling parameters are summarized in the [Supplementary Table S1](#).

## 2.1. Electrochemistry

### 2.1.1. Li diffusion within the active material

The mass conservation states



**Fig. 1.** (a) Schematics of co-evolving electrochemistry and mechanical damage in a NMC composite cathode under galvanostatic charging. Five electrochemical processes are considered: (I) Li diffusion within the active materials, (II) interfacial charge transfer at the original interface between the electrode and the electrolyte, (III) interfacial charge transfer at the freshly fractured surfaces, (IV) electron conduction in the carbon-binder matrix, and (V) Li transport in the electrolyte. Depending on the severity, mechanical damage is considered as (1) minor cracks, (2) major cracks, or (3) complete cracks that isolate NMC primary particles. (b) The simplified computational geometry of a half cell includes a current collector at the bottom, an active NMC particle surrounded by a porous carbon binder domain filled with electrolyte (light blue color), a separator (dark blue color), and a Li metal anode at the top. (For interpretation of the references to color in this figure legend, the reader is referred to the Web version of this article.)

$$\frac{\partial c}{\partial t} = -j_{i,i}, \quad (1)$$

where  $c$  is Li concentration in the active material, and  $j_i$  is the flux. Here, the tensor convention is followed and  $j_{i,i}$  means the divergence operation. Fick's law describes Li diffusion kinetics in the active particles,

$$j_i = -\frac{c}{RT} D_{ij} \mu_{,j}, \quad (2)$$

where  $D_{ij}$  represents Li diffusivity ( $2^{\text{nd}}$ -order tensor),  $\mu$  is the chemical potential of Li,  $\mu_{,j}$  is the gradient of  $\mu$ ,  $R$  is the gas constant, and  $T$  is the temperature. We use Larché and Cahn's model [36] to define the internal energy density. Only the contribution of chemical and mechanical energies inside the active particles is considered. Hence, the differential of the internal energy density  $e$  yields

$$de = \sigma_{ij} d\epsilon_{ij} + \mu dc, \quad (3)$$

where  $\sigma_{ij}$  and  $\epsilon_{ij}$  are the stress and strain tensors, respectively. By differentiating  $e - \sigma_{ij} \epsilon_{ij}$ , it gives

$$d(e - \sigma_{ij} \epsilon_{ij}) = de - \sigma_{ij} d\epsilon_{ij} - \epsilon_{ij} d\sigma_{ij}. \quad (4)$$

And plugging Eq. (3) into Eq. (4) yields

$$d(e - \sigma_{ij} \epsilon_{ij}) = \mu dc - \epsilon_{ij} d\sigma_{ij}. \quad (5)$$

According to the Clairaut's theorem, if the second partial derivative of a function is continuous, the order of differentiation is immaterial,  $Q_{ij} = Q_{ji}$ . Therefore, the result of differentiating  $e - \sigma_{ij} \epsilon_{ij}$  first by  $\sigma_{ij}$  then by  $c$  should be equal to differentiating it first by  $c$  then by  $\sigma_{ij}$ ,

$$\left( \frac{\partial \epsilon_{ij}}{\partial c} \right)_{\sigma_{ij}} = - \left( \frac{\partial \mu}{\partial \sigma_{ij}} \right)_c. \quad (6)$$

For NMC, the inelastic deformation is not considered. The total strain is composed of the chemical strain  $\epsilon_{ij}^C$  and the elastic strain  $\epsilon_{ij}^E$ ,

$$\epsilon_{ij} = \epsilon_{ij}^C + \epsilon_{ij}^E. \quad (7)$$

The (de)lithiation-induced chemical strain  $\epsilon_{ij}^C$  is calculated as

$$\varepsilon_{ij}^C = \begin{bmatrix} \frac{l_a - l_{a0}}{l_{a0}} & 0 & 0 \\ 0 & \frac{l_a - l_{a0}}{l_{a0}} & 0 \\ 0 & 0 & \frac{l_c - l_{c0}}{l_{c0}} \end{bmatrix}, \quad (8)$$

where  $l_a$  and  $l_c$  are the lattice parameters along the  $a$  and  $c$ -axis at a given state of charge (SOC) and  $l_{a0}$  and  $l_{c0}$  are at the pristine state, respectively. NMC has a hexagonal layered lattice structure. We use anisotropic elasticity to model the mechanical behavior. The constitutive law describes the relationship between the elastic strain  $\varepsilon_{ij}^E$  and stress:

$$\varepsilon_{ij}^E = S_{ijkl} \sigma_{kl}. \quad (9)$$

where  $S_{ijkl}$  represents the inverse of the stiffness of NMC, which depends on the Li concentration  $c$ . We expand the term  $\left(\frac{\partial \varepsilon_{ij}}{\partial c}\right)_{\sigma_{ij}}$  as follows:

$$\left(\frac{\partial \varepsilon_{ij}}{\partial c}\right)_{\sigma_{ij}} = \frac{\partial \varepsilon_{ij}^C}{\partial c} + \frac{\partial \varepsilon_{ij}^E}{\partial c} = \beta_{ij} + \frac{dS_{ijkl}}{dc} \sigma_{kl}, \quad (10)$$

where the 2<sup>nd</sup>-order tensor  $\beta_{ij}$  represents the anisotropic chemical expansion coefficient. By plugging Eq. (10) into Eq. (6), it yields

$$\left(\frac{\partial \mu}{\partial \sigma_{ij}}\right)_c = -\beta_{ij} - \frac{dS_{ijkl}}{dc} \sigma_{kl}. \quad (11)$$

By multiplying  $d\sigma_{ij}$  on both sides of Eq. (11), the differential of chemical potential is expressed as

$$d\mu = -\beta_{ij} d\sigma_{ij} - \left(\frac{dS_{ijkl}}{dc} \sigma_{kl}\right) d\sigma_{ij}. \quad (12)$$

By integrating Eq. (12), it gets

$$\mu = M(c) - \beta_{ij} \sigma_{ij} - \frac{1}{2} \frac{dS_{ijkl}}{dc} \sigma_{ij} \sigma_{kl}, \quad (13)$$

where  $M(c)$  is a function of  $c$  only. The chemical potential  $\mu$  is finally obtained as

$$\mu = \mu_0 + RT \ln\left(\gamma \frac{\bar{c}}{1 - \bar{c}}\right) - \beta_{ij} \sigma_{ij} - \frac{1}{2} \frac{dS_{ijkl}}{dc} \sigma_{ij} \sigma_{kl}, \quad (14)$$

where  $\mu_0$  is a reference potential,  $\gamma$  is the thermodynamic activity coefficient, and  $\bar{c}$  is the normalized Li concentration.

At the outer surface of the active particle, Li flux is related to the interfacial charge transfer current density  $i_{BV}$  by

$$j_i n_i^p = -\frac{i_{BV}}{F}, \quad (15)$$

where  $n_i^p$  is the unit normal vector pointing from the electrolyte domain towards the active particle,  $i_{BV}$  is the interfacial charge transfer current calculated from the Butler-Volmer equation, and  $F$  is the Faraday constant.

The chemical potential in Eq. (14) consists of the following material parameters: the activity coefficient  $\gamma$ , the anisotropic chemical expansion coefficients  $\beta_{ij}$ , and the derivative of compliance coefficients  $\frac{dS_{ijkl}}{dc}$ . The three sets of material parameters are determined as follows. The activity coefficient  $\gamma$  accounts for the nonideality effect when the solid solution is not dilute. It is obtained by fitting the open-circuit potential of NMC against Li using a polynomial function  $RT \ln \gamma = \sum_{k=2}^N \Omega_k k \bar{c}^{k-1}$ , and the open-circuit potential is expressed as follows [17,18],

$$FU = FU_0 + RT \ln\left(\frac{1 - \bar{c}}{\bar{c}}\right) - RT \ln \gamma, \quad (16)$$

where  $U$  is the open-circuit potential,  $U_0$  is the reference open-circuit potential, and  $\Omega_k$  is the self-interaction coefficient characterizing interaction between Li atoms. The blue triangles in Fig. 2(a) are the experimental data of the open-circuit potential  $U$  for LiNi<sub>0.8</sub>Mn<sub>0.1</sub>Co<sub>0.1</sub>O<sub>2</sub> (NMC811) [8]. The black line shows the polynomial fitting curve up to the 6<sup>th</sup> order. The Supplementary Table S2 lists the self-interaction coefficients and the reference open-circuit potential  $U_0$ . We may evaluate the effect of the activity coefficient on diffusion in the following equation (where the mechanical potential is not accounted):

$$\frac{\partial \bar{c}}{\partial t} = \left(\frac{D_{ij}}{1 - \bar{c}} \left(1 + \frac{(1 - \bar{c}) \bar{c}}{\gamma} \frac{d\gamma}{d\bar{c}}\right) \bar{c}_{,j}\right)_{,i}, \quad (17)$$

in which  $\frac{(1 - \bar{c}) \bar{c}}{\gamma} \frac{d\gamma}{d\bar{c}}$  is due to the dependence of the activity coefficient on Li concentration. This function is plotted in Fig. 2(a) in the red line. It is zero when the active material is fully lithiated or delithiated, however, it largely deviates from zero at other states of charge which promotes Li diffusion. For instance, at  $x = 0.4$ , the nonideality effect  $\frac{(1 - \bar{c}) \bar{c}}{\gamma} \frac{d\gamma}{d\bar{c}} = 9$ , showing that the effective Li diffusivity is about one order of magnitude higher than the intrinsic diffusivity.

The black curves in Fig. 2(b) denote the experimental data of  $l_a$  (lattice parameter along the  $a$ -axis) and  $l_c$  (lattice parameter along the  $c$ -axis) from operando synchrotron X-ray diffraction (XRD) as a function of Li fraction  $x$  in NMC811 [8]. The chemical strain  $\varepsilon_{ij}^C$  is then calculated using Eq. (8). The red curves show the anisotropic chemical expansion coefficients  $\beta_{ij}$  obtained from the derivative of the chemical strains with respect to the Li concentration,  $\beta_{ij} = \left(\frac{\partial \varepsilon_{ij}^C}{\partial c}\right)$ .

The Supplementary Table S3 lists the values of stiffness coefficients  $C_{ijkl}$  as a function of fraction  $x$  in NMC811 calculated by first-principles modeling from an unpublished work [37]. By inverting the stiffness matrix, we obtain the compliance matrix  $S_{ijkl}$  denoted as triangles in Fig. 2(c). The linear fitting curves of the compliance coefficients are used to calculate  $\frac{dS_{ijkl}}{dc}$ .

### 2.1.2. Interfacial charge transfer

The interfacial charge transfer reaction  $Li \leftrightarrow Li^+ + e^-$  at the interface between the active material and the electrolyte is described by the Butler-Volmer (BV) equation,

$$i_{BV} = i_0 \left( e^{\frac{\alpha_a F \eta}{RT}} - e^{-\frac{\alpha_c F \eta}{RT}} \right), \quad (18)$$

where  $i_{BV}$  is the local current density,  $\alpha_a$  the anodic transfer coefficient,  $\alpha_c$  the cathodic transfer coefficient, and  $i_0$  the exchange current density which is defined as

$$i_0 = F(k_c)^{\alpha_c} (k_a)^{\alpha_a} (c_{\max} - c)^{\alpha_a} c^{\alpha_c} \left(\frac{c^1}{c_{\text{ref}}^1}\right)^{\alpha_a}, \quad (19)$$

where  $k_c$  and  $k_a$  are the rate constants for the cathodic and anodic reactions,  $c$  and  $c_{\max}$  are the current and max Li concentrations in the active material, respectively.  $c^1$  and  $c_{\text{ref}}^1$  are the current and reference Li-ion concentrations in the electrolyte, respectively.  $\eta$  in Eq. (18) denotes the overpotential,

$$\eta = \varphi^c - \varphi^l - E_{\text{eq}}, \quad (20)$$

where  $\varphi^c$  is the electric potential at the surface,  $\varphi^l$  is the electrolyte potential, and  $E_{\text{eq}}$  is the equilibrium potential of Li in the active material at a given state of charge which is measured from experiments [8]. Our previous work demonstrates that the stress effect on the overpotential is insignificant [12], therefore, it has been neglected in this work.

When intergranular cracks emerge, liquid electrolyte infiltrates along the grain boundaries into the freshly exposed interior region of NMC polycrystalline particles. Like the outer surface of the NMC parti-

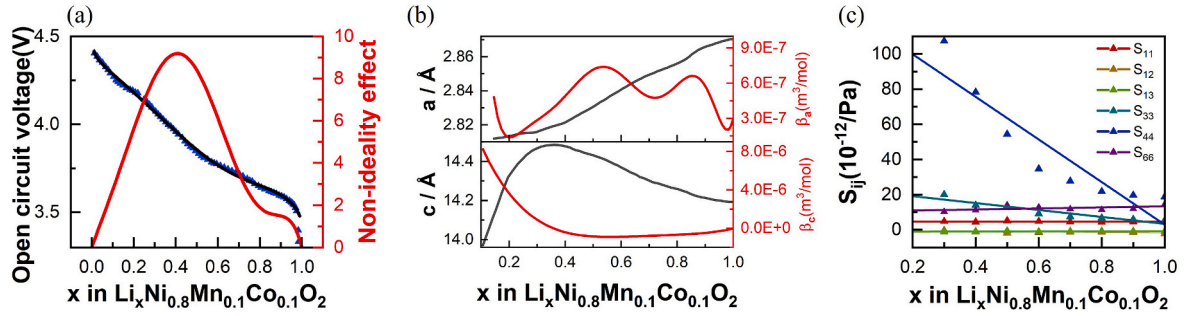


Fig. 2. Material properties adopted in the modeling. (a) An experimental measurement of the open-circuit voltage of NMC811 against Li (blue triangles) reported by Marker et al. [8] The black line (overlapping with the blue dots) is the fitting curve of the experimental data using a polynomial function, and the red line represents the derivative term of the thermodynamic activity coefficient in Eq. (17). (b) Experimental measurements (black lines) of lattice parameters in the  $a$ - and  $c$ -axis upon (de)lithiation reported by Marker et al. The anisotropic chemical expansion coefficients  $\beta_a$  and  $\beta_c$  (red lines) are calculated based on the lattice parameters. (c) The anisotropic compliance coefficients of NMC811, which is calculated based on the first-principles modeling [37]. The dots represent atomistic simulation data, and the solid lines represent fitting functions used in the current modeling. (For interpretation of the references to color in this figure legend, the reader is referred to the Web version of this article.)

cle, interfacial charge transfer occurs at these fractured surfaces. Electrolyte infiltration can be depicted as liquid movement in a capillary. The Supplementary Fig. S1(a) shows the schematic of the capillary motion, described by the Washburn equation [38],

$$l = \sqrt{\frac{\bar{r}_{\text{eff}} \Gamma \cos \theta}{2\nu}} \sqrt{t}, \quad (21)$$

where  $l$  is the infiltration length at time  $t$ ,  $\bar{r}_{\text{eff}}$  is the effective capillary radius,  $\Gamma$  is the surface tension,  $\theta$  is the contact angle, and  $\nu$  is the viscosity. Fig. S1(b) shows the geometry of electrolyte infiltration through the freshly exposed surface of the NMC particle. We adopt the damage initiation displacement  $u_0$  as the effective radius  $\bar{r}_{\text{eff}}$  and the particle radius as the infiltration length  $l$  to estimate the order of the infiltration time  $t$ . The parameters  $\Gamma$ ,  $\theta$ , and  $\nu$  for  $\text{LiNi}_{0.5}\text{Mn}_{0.3}\text{Ni}_{0.2}\text{O}_2$  (NMC532) with a typical carbonate-based electrolyte have been measured by experiments [39]. By plugging the parameters in Eq. (21), we determine that the infiltration time  $t$  of the liquid electrolyte penetration in the NMC secondary particle is about 5 ms, which is several orders of magnitude smaller than the charging time. Hence, we can ignore the dynamic process of liquid infiltration and assume an equilibrium state of electrolyte penetration along the grain boundaries as soon as mechanical damage initiates and the fractured surface becomes accessible to the liquid electrolyte.

We obtain the local field variables  $\hat{c}'_i$ ,  $\hat{\phi}'_i$ , and  $\hat{\varphi}'_c$  at the freshly fractured internal surface by calculating the average of these values nearby the electrolyte-NMC interfaces. If the normal displacement ( $d_n$ ) between two neighboring elements is larger than the damage initiation displacement ( $d_0$ ), we use a modified Butler-Volmer equation as a flux boundary condition at the fractured surface,

$$\begin{aligned} \hat{i}_{BV} &= \hat{i}_0 \left( e^{\frac{\alpha_a F \eta}{RT}} - e^{-\frac{\alpha_c F \eta}{RT}} \right), \\ \hat{i}_0 &= F(k_c)^{\alpha_a} (k_a)^{\alpha_c} (c_{\text{max}} - c_s)^{\alpha_a} (c_s)^{\alpha_c} \left( \frac{\hat{c}'_l}{c_{l, \text{ref}}} \right)^{\alpha_a}, \\ \eta &= \hat{\varphi}'_c - \hat{\phi}'_l - E_{\text{eq}}. \end{aligned} \quad (22)$$

The normal displacement ( $d_n$ ) and the damage initiation displacement ( $d_0$ ) are defined in Section 2.3.

### 2.1.3. Electron conduction in the carbon-binder matrix

Ohm's law describes electron conduction in the conductive matrix,

$$\hat{i}'_i = -K^c \hat{\varphi}'_{i,i}, \quad (23)$$

where  $\hat{i}'_i$  is the electric current density,  $K^c$  is the electrical conductivity of the carbon-binder matrix. The charge conservation states

$$\hat{i}'_{i,i} = 0. \quad (24)$$

We define the unit normal vectors pointing from the cathode to the current collector as  $\hat{n}_i^{\text{cc}}$ , from the cathode to the separator as  $\hat{n}_i^{\text{cs}}$ , and from the model to the outside as  $\hat{n}_i^{\text{s}}$ . The boundary conditions are following:

$$\begin{aligned} \hat{i}'_i \hat{n}_i^{\text{cc}} &= -i_{\text{app}} \text{ at } y = 0; \\ \hat{i}'_i \hat{n}_i^{\text{cs}} &= 0 \text{ at } y = L; \\ \hat{i}'_i \hat{n}_i^{\text{s}} &= 0 \text{ at } x = 0 \text{ and } x = W. \end{aligned} \quad (25)$$

$i_{\text{app}}$  represents the externally applied current density during the galvanostatic charging or discharging.  $i_{\text{app}}$  is calculated based on the charging rate ( $C_{\text{rate}}$ ), maximum Li concentration ( $c_{\text{max}}$ ), active particle radius ( $r$ ), and the current collector width ( $W$ ):

$$i_{\text{app}} = \frac{C_{\text{rate}}}{1h} \times \frac{F \times c_{\text{max}} \times \pi r^2}{W}. \quad (26)$$

When the cell is cycled at a given  $C_{\text{rate}}$ , it takes  $\frac{1}{C_{\text{rate}}}$  hours for the cell to be fully charged or discharged. At the boundaries between the active particle and the electrolyte, the electric current density is determined by

$$\hat{i}'_i \hat{n}_i^{\text{p}} = i_{\text{BV}}. \quad (27)$$

### 2.1.4. Li-ion diffusion in the electrolyte

The concentration gradient and the electric field drive the transport of charged Li ions in the electrolyte. The flux  $j_i^l$  is determined by

$$j_i^l = -D^l c_i^l + \frac{t_+}{F} \hat{i}'_i, \quad (28)$$

where  $D^l$  is the diffusivity of Li ions in the electrolyte,  $c^l$  is the Li-ion concentration in the electrolyte,  $t_+$  is the transference number of the cation ( $\text{Li}^+$ ). Newman et al. [40] derived the electrolyte current density  $\hat{i}'_i$  as

$$\hat{i}'_i = -K^l \hat{\varphi}'_{i,i} + \frac{2K^l RT}{F} \left( 1 + \frac{\partial \ln f}{\partial c^l} \right) (1 - t_+) (\ln c^l)_{,i}, \quad (29)$$

where  $K^l$  is the electrolyte ionic conductivity,  $\hat{\varphi}^l$  is the electrolyte potential, and  $f$  is the mean activity of the electrolyte. The charge carriers in the electrolyte obey the conservation laws,

$$\frac{\partial c^l}{\partial t} = -j_{i,i}^l, \quad (30)$$

and

$$i_{i,i}^l = 0. \quad (31)$$

The insulation and zero-flux boundary conditions are applied at  $x = 0$ ,  $x = W$ , and  $y = 0$ ,

$$\begin{aligned} i_i^{l,cc} &= 0 \text{ at } y = 0; \\ i_i^{l,s} &= 0 \text{ at } x = 0 \text{ and } x = W; \\ j_i^{l,cc} &= 0 \text{ at } y = 0; \\ j_i^{l,s} &= 0 \text{ at } x = 0 \text{ and } x = W; \end{aligned} \quad (32)$$

At the boundary between the separator and the anode Li metal, a robin boundary condition is applied as follows,

$$\begin{aligned} i_i^{l,sa} &= \bar{i}^{sa} \text{ at } y = L + L_s; \\ j_i^{l,sa} &= \frac{\bar{i}^{sa}}{F} \text{ at } y = L + L_s. \end{aligned} \quad (33)$$

where  $n_i^{sa}$  is the unit normal vector pointing from the separator to the anode Li metal.  $\bar{i}^{sa}$  is the local charge transfer current density governed by the Butler-Volmer equation,

$$\begin{aligned} i^{sa} &= i_0^{sa} \left( e^{\frac{a_a F \eta^{sa}}{RT}} - e^{-\frac{a_c F \eta^{sa}}{RT}} \right); \\ i_0^{sa} &= i_{0,ref}^{sa} \left( \frac{c^l}{c_{ref}^l} \right)^{\alpha_a}; \\ \eta^{sa} &= \varphi^{c,ext} - \varphi^l - E_{eq}^{Li}. \end{aligned} \quad (34)$$

$i_{0,ref}^{sa}$  is the reference current density,  $\varphi^{c,ext}$  is the externally applied electric potential, and  $E_{eq}^{Li}$  is the equilibrium potential of Li metal (0 V). The anode Li metal is connected to the ground, therefore,

$$\varphi^{c,ext} = 0 \text{ at } y = L + L_s. \quad (35)$$

At the boundaries between the NMC active particle and the electrolyte, the electric current density is determined by

$$i_i^{l,p} = -i_{BV}, \quad (36)$$

and the Li-ion flux is determined by

$$j_i^{l,p} = -\frac{i_{BV}}{F}. \quad (37)$$

## 2.2. Mechanics

Mechanical deformation and the stress field in the porous cathode composite are determined by solving the elastic boundary-value problem. We adopt the plane strain assumption. Mechanical equilibrium is established much faster than Li diffusion, therefore,

$$\sigma_{ij,j} = 0. \quad (38)$$

We assume a linear elastic behavior of the electrolyte and carbon-binder domain and its elastic modulus was measured as around 5 GPa in our previous work [41]. For the NMC active particle, the elastic constitutive equation describes the stress-strain relationship,

$$\sigma_{ij} = C_{ijkl} \varepsilon_{kl}^E, \quad (39)$$

where  $\sigma_{ij}$  is the stress tensor,  $\varepsilon_{kl}^E$  is the elastic strain, and  $C_{ijkl}$  is the stiffness matrix. Recalling Eq. (7), the total strain consists of the chemical strain  $\varepsilon_{ij}^C$  and the elastic strain  $\varepsilon_{ij}^E$ . The total strains  $\varepsilon_{ij}$  are related to the displacements  $u_i$  as

$$\varepsilon_{ij} = \frac{1}{2} (u_{i,j} + u_{j,i}). \quad (40)$$

The displacive conditions are prescribed as follows,

$$\begin{aligned} u_i n_i^{cc} &= 0 \text{ at } y = 0; \\ u_i n_i^{cs} &= 0 \text{ at } y = L; \\ u_i n_i^s &= 0 \text{ at } x = 0 \text{ and } x = W. \end{aligned} \quad (41)$$

## 2.3. Mechanical damage

Using the cohesive zone model (Supplementary Fig. S1(c)), we simulate crack initiation and growth at the grain boundaries between the neighboring primary particles. The boundary elements are undamaged when the normal displacement ( $d_n$ ) is smaller than the damage initiation displacement ( $d_0$ ), i.e.,  $d_n < d_0$ , and the normal traction ( $t_n$ ) at the boundary is proportional to the normal displacement,

$$t_n = K_n d_n, \quad (42)$$

where  $K_n$  is the normal stiffness of the cohesive element. Damage initiates when  $t_n > t_0$ , where  $t_0$  is the interfacial strength. The failure initiation displacement  $d_0$  is defined as  $d_0 = \frac{t_0}{K_n}$ . The cohesion of the boundaries is considered fully damaged when the energy release rate ( $G$ ) of the cohesive elements equals or exceeds the fracture energy  $\Gamma$ . The failure displacement  $d_f$  is calculated as  $d_f = \frac{2\Gamma}{t_0}$ . When damage propagates,  $d_0 < d_n < d_f$ , the normal traction is proportional to the normal displacement, and the reduced stiffness  $t_n = (1 - D)K_n d_n$ . After the boundary is fully damaged, there is no traction between the neighboring grains. The damage function  $D$  is determined by

$$D = \begin{cases} 0, & d_n < d_0 \\ \frac{d_f}{d_n} \left( \frac{d_n - d_0}{d_f - d_0} \right), & d_0 < d_n < d_f \\ 1, & d_n > d_f \end{cases} \quad (43)$$

The maximum damage value at all the boundaries is stored at each time step to ensure that the damage is non-recoverable, i.e., even if the normal displacement becomes zero during subsequent steps, the damage value remains the maximum of its historical values. To clarify, we only consider crack opening along the grain boundaries, and we set the shear strength as infinite in the cohesive zone model.

## 2.4. Electrolyte infiltration along the fractured surfaces and its consequence

Upon the intergranular fracture, liquid electrolyte infiltrates along the grain boundaries into the interior region of the NMC polycrystalline particle. Such processes incur side reactions and TM ions dissolutions between the electrolyte and the newly exposed surface. We term the resulting side reactions and ion dissolution as the corrosion effect, which generally weakens the mechanical cohesion between the primary particles. In the numerical modeling, we assume that the magnitude of the fracture strength and fracture energy of the corroded surfaces are half of the original values [42]. Meanwhile, even though the freshly exposed surfaces increase the surface area for the interfacial reaction, the low electrical conductivity of NMC [43] impedes electron conduction along the cracked surfaces when not in contact with the conductive matrix. Here, we mimic the impedance of electron conduction as a penalty factor in the interfacial charge transfer kinetics at the fractured surfaces. The detailed implementation is described as follows.

### 2.4.1. Corrosion

We previously studied the corrosive behavior of intergranular fracture of NMC cathode, where the fracture strength of the cohesive elements decreases during charging and as the cycle proceeds [44]. To implement the corrosion effect due to electrolyte infiltration, we assume that the fracture strength  $t_c$  and the fracture energy  $\Gamma_c$  of the corroded boundaries are half of the original intact boundaries,

$$\begin{aligned} t_c &= \frac{1}{2}t_0, \\ \Gamma_c &= \frac{1}{2}\Gamma_0. \end{aligned} \quad (44)$$

As shown in the [Supplementary Fig. S1\(c\)](#), the area of the blue triangle represents the original fracture energy  $\Gamma_0$  and the orange triangle is the reduced fracture energy  $\Gamma_c$ . It is worth noting that the choice of the reduced fracture strength and fracture energy is simply for the demonstration purpose of numerical modeling. There is no experimental report of their values in literature.

#### 2.4.2. Penalty to ion transport and electron conduction

Li flux at the fractured surface is calculated by the Butler-Volmer equation using two penalty factors,  $PF_{ion}$  and  $PF_e$ . The actual ion flux at the fractured surface is calculated as  $PF_{ion}$  multiplying by the value from the BV equation, which mimics the impedance of Li ions transport due to the surface phase transformation or the cathode-electrolyte interface (CEI) formation. Measuring  $PF_{ion}$  in experiments is challenging; hence we perform a parametric study for three values of  $PF_{ion} = 1, 0.5, \text{ and } 0.1$ . The results are summarized in the [Supplementary Fig. S2](#). We find that the damage pattern and extension at the end of the first charging are nearly the same with the three values, except Li distributions are different because of the modulated interfacial charge transfer kinetics. We choose  $PF_{ion} = 0.1$  in the following numerical modeling.  $PF_e$  corresponds to the reduced electron flow from the infiltrated surface to the matrix due to the low electrical conductivity of the freshly exposed NMC. When a primary particle has more damaged grain boundaries, it has less channels to pass electrons to the neighboring particles and to the conductive network. Therefore, the penalty factor  $PF_e$  is calculated based on the degree of mechanical damage of a given primary particle,

$$PF_e = 1 - 1.25d_{avg}, \quad (45)$$

where  $d_{avg}$  is the average damage of the cohesive elements surrounding the primary particle. We assume that once the boundary conditions around a primary particle are 80% damaged ( $d_{avg} = 0.8$ ), the electron conduction pathway is fully disrupted, and Li-ion flux ( $j_i$ ) at the fractured surface reduces to zero. This equation is chosen for the purpose of demonstration of computational modeling, to our best knowledge, without prior experimental validation. We consider that electron flow is coupled with the intergranular fracture – in the extreme case when 80% of the electron path surrounding a primary particle is damaged, the primary particle is isolated from the electron conducting network.

Overall, Li-ion flux  $j_i$  at the freshly fractured surfaces is calculated by a modified Butler-Volmer equation.

$$j_i n_i^{fs} = -\frac{PF_{ion} \times PF_e \times i_{BV}^i}{F}, \quad (46)$$

where  $n_i^{fs}$  is the unit normal vector at the fractured surface pointing towards the active material and  $i_{BV}^i$  is calculated from Eq. (22). The sum of the total interfacial flux at the NMC outer surface and the freshly fractured surfaces remains equal to the externally applied total current  $i_{app} \times W$  at the current collector,

$$-i_{app} \times W = F \int_{\Omega_{ext}} j_i n_i^p dS + F \int_{\Omega_{fs}} j_i n_i^{fs} dS, \quad (47)$$

## 3. Results and discussion

### 3.1. The anisotropic material properties

To underscore the critical role of the anisotropic transport and mechanical properties in predicting the chemomechanical behavior of the NMC cathode, we use a single NMC polycrystalline particle as a

demonstration and prescribe a constant flux boundary condition at the outer surface [38]. In this section, we primarily evaluate the anisotropic material properties, while the effect of the mechanical potential on Li diffusion is demonstrated in the next section. To illustrate the effect of anisotropic material properties, we adopt isotropic diffusivity, isotropic mechanical properties, and isotropic chemical strains for the isotropic model, while anisotropic diffusivity, anisotropic mechanical properties, and anisotropic chemical strains are considered for the anisotropic model. Li diffusivity is a 2nd-order tensor in the diffusion equation,

$$\frac{\partial c}{\partial t} = D_{ij} c_{,ij}, \quad (48)$$

and because of the hexagonal symmetry, Li diffusivity can be reduced to the following form in the 2D case,

$$D_{ij} = \begin{bmatrix} D_{ab} & 0 \\ 0 & D_c \end{bmatrix}, \quad (49)$$

where  $D_{ab}$  is the Li diffusivity along the  $a$ - and  $b$ -axis and  $D_c$  along the  $c$ -axis. To make a comparison between the isotropic and anisotropic models, we need to choose an effective diffusion coefficient for the isotropic model. The effective diffusion coefficient depends on the microstructure of the secondary particles such as grain size and orientations. To obtain the effective diffusivity, we consider the ideal case where the grain orientation in the polycrystal is entirely stochastic and diffusion along the  $c$ -axis is negligible compared to the  $ab$ -plane. Then, for each grain with an orientation angle  $\theta$  ( $\theta = 0$  corresponding to Li diffusion along the  $ab$ -plane), the effective diffusivity is  $D_{ab} \cos \theta$ . And the average effective diffusivity of the polycrystal can be calculated as

$$D_{eff} = \frac{\int_0^{\frac{\pi}{2}} D_{ab} \cos \theta d\theta}{\int_0^{\frac{\pi}{2}} d\theta} = \frac{2}{\pi} D_{ab}.$$

In the anisotropic model, we assume  $D_c = \frac{1}{10} D_{ab}$  while the anisotropic effect becomes more significant when the ratio becomes larger. To focus on the primary effect of anisotropy, we do not consider the change of diffusivity at different states of charge [45]. For the mechanical property, we adopt the calculated stiffness constants  $C_{ijkl}$  [37], which are summarized in the [Supplementary Table S3](#). In the reference, the effective isotropic mechanical properties are obtained using the Voigt-Reuss scheme [46]. Lastly, for the anisotropic deformation, NMC lattice parameters upon (dis)charging are obtained from the experimental data, and chemical strains are calculated by Eq. (8). In the reference isotropic model, the chemical strain  $\epsilon_{ij}^c$  is calculated from the volume change of NMC upon (dis)charging, and  $\epsilon_{ij}^c = \left( \sqrt{3\frac{V}{V_0}} - 1 \right) \delta_{ij}$ , where  $V$  and  $V_0$  are the volume of NMC lattice at a given state of charge and in the pristine state, respectively [8]. A constant flux  $J_0$  is applied on the boundary of the particle to mimic the 1C charging condition.

[Fig. 3\(a\)](#) shows the isotropic model. [Fig. 3\(d\)](#) shows the anisotropic model with random grain orientations, which is generated using a random function, ranging from  $-\pi$  to  $\pi$ , where the inset coordinate indicates the reference orientations of  $a$ -axis and  $c$ -axis as zero degree. [Fig. 3\(b\)](#) and (e) show the profiles of the normalized Li concentration ( $\bar{c}$ ) in the isotropic and anisotropic models at  $t = 1800s$ , corresponding to the state of charge of 0.5 during the first charging. In the isotropic case, Li concentration shows the core-shell pattern, and its gradient is present only along the radial direction. Such radial heterogeneity is caused by the low Li diffusivity at a fast-charging rate. In comparison, anisotropic diffusivity ( $D_{ij}$ ) generates a much higher radial as well as angular concentration heterogeneity due to the tortuous Li diffusion pathways induced by the random orientation of primary particles. Such spatial variation in concentration has multifold effects since both the electrochemical and mechanical responses of NMC are dependent on the SOC ([Fig. 2](#)). [Fig. 3\(c\)](#) and (f) show the hoop stress profile within the secondary particle at  $t = 1800s$ . During the charging process, Li is extracted from the particle and the lattice volume shrinks. The isotropic model

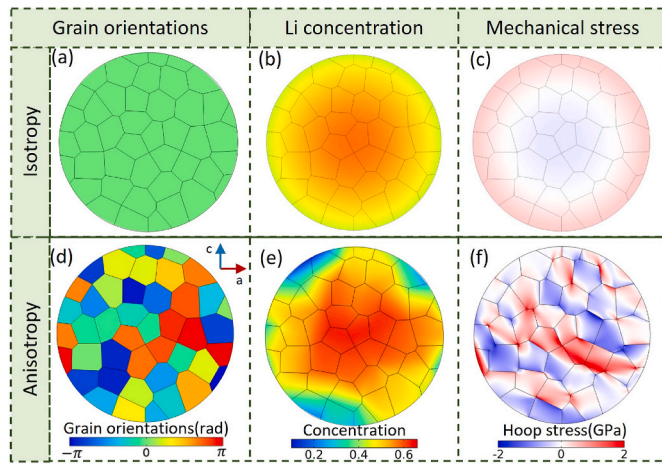


**Fig. 3.** Demonstration of the effects of anisotropic Li diffusivity, anisotropic mechanical property, and anisotropic chemical strains on Li distribution and mechanical stresses in the NMC secondary particle. The grain orientations, Li concentration, and mechanical stress distribution are shown for the isotropic (top row) and anisotropic (bottom row) model.

predicts a stress pattern where the outer shell is in tension and the core under compression. Such symmetry is broken in the anisotropic model and the magnitude of stresses is much higher due to the mismatch strains between two disorientated neighboring primary particles. Stress is the primary driving force of crack initiation and propagation. Both the concentration heterogeneity and strain localization at the grain boundaries contribute to the large stress field within the NMC polycrystalline particle. Herein, we demonstrate that the anisotropic diffusivity, anisotropic mechanical property, and anisotropic chemical strains are the essential features to be included to understand the chemomechanical behavior of layered oxide electrodes.

### 3.2. Mechanical potential on the diffusion kinetics

In this section, we evaluate the effect of mechanical potential on Li diffusion kinetics and determine the importance of coupling in the numerical modeling. We build a 2D half-cell model and apply the fully coupled electrochemo-mechanics theory as described in Sections 2.1 and 2.2. The half-cell model is subject to a galvanostatic charging and discharging cycle at 1C. We first apply a positive current to the current collector of the NMC cathode until the upper cutoff voltage 4.25 V is reached, and then reverse the applied current until the voltage drops to the lower cutoff voltage of 3.55 V. By plugging the chemical potential (Eq. (14)) into the Fick's law (Eq. (2)), we obtain

$$j_i = -\frac{c}{RT}D_{ij}\left(RT \ln \frac{\bar{c}}{1-\bar{c}}\right)_j - \frac{c}{RT}D_{ij}(RT \ln \gamma)_j + \frac{c}{RT}D_{ij}(\beta_{kl}\sigma_{kl})_j + \frac{c}{RT}D_{ij}\left(\frac{1}{2}\frac{dS_{mnl}}{dc}\sigma_{mn}\sigma_{kl}\right)_j, \quad (50)$$

where  $RT \ln \frac{\bar{c}}{1-\bar{c}}$  represents the entropic contribution in the chemical potential,  $RT \ln \gamma$  the contribution from the solution nonideality, and the last two terms represent the contribution from the mechanical potential where  $\beta_{kl}\sigma_{kl}$  may be named as a stress potential, and  $\frac{1}{2}\frac{dS_{mnl}}{dc}\sigma_{mn}\sigma_{kl}$  represents the contribution by the change of material stiffness upon (dis)charging. Fig. 4(a) shows the voltage responses with (red dots) and without (black lines) considering the mechanical potential (the last two terms in Eq. (50)). The two curves are nearly overlapping indicating that the voltage measure does not differentiate the mechanical effect. However, Li distribution is indeed impacted by the mechanical potential. Fig. 4(b) and (c) show the Li concentration profiles without and with the mechanical effect at the end of the first charging. Li distribution shows a more uniform pattern without considering the mechanical driving force

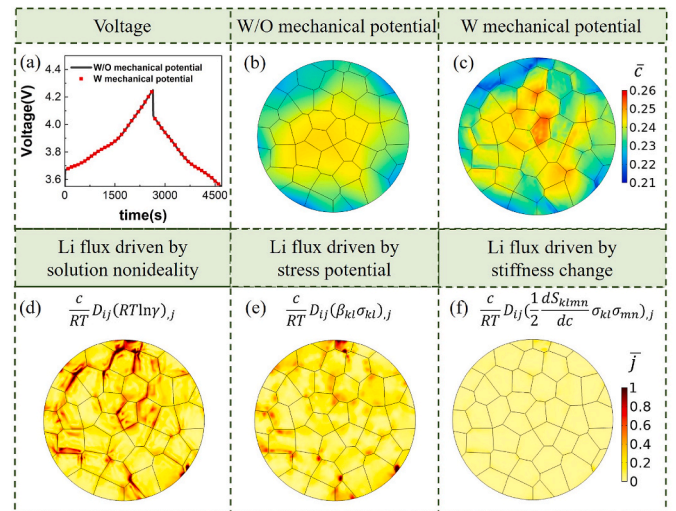


**Fig. 4.** Demonstration of the mechanical effect on electrochemical responses. (a) Voltage curves of the NMC cathode against Li with and without considering the mechanical potential on Li diffusion at 1C charging rate. The two curves are nearly overlapping. In terms of Li distribution, at the end of first charging, Li concentration is more uniform without considering the mechanical potential (b) while its distribution is more heterogeneous when the mechanical effect is considered (c). A quantitative comparison of Li flux driven by (d) solution nonideality, (e) the stress potential, and (f) change of the mechanical stiffness at the end of the first charging.

in diffusion, while it becomes more heterogeneous when the mechanical potential is incorporated. This is in contrast to the feature that mechanical stresses tend to homogenize the diffusive species in the host, and such difference is caused by the geometric effect of the polycrystalline configuration. In a secondary particle, the anisotropic deformation and random orientations of the constituent particles induce localized stresses at the grain boundaries throughout the particle. Thus, the mechanical potential, which is a function of the local stress, is heterogeneously distributed and results in the high heterogeneity of Li distribution in the polycrystalline particle.

Fig. 4(d)–(f) provide a quantitative comparison of the relative contributions towards the Li flux from the three terms in Eq. (50). The solution nonideality contributes the highest magnitude of Li flux, Fig. 4(d), while the stress potential adds more heterogeneity in Li distribution, but the effect is relatively small. The contribution from the change of the mechanical stiffness is negligible (Fig. 4(f)). The comparison demonstrates that the thermodynamics in the Li-concentrated solution dominates the diffusion kinetics. Overall, the mechanical potential does influence Li distribution within the polycrystalline particle but not the voltage response which is predominantly determined by the interfacial charge transfer kinetics at the surface of the particle [12]. We further examine the influence of mechanical potential at multiple charging rates (Supplementary Fig. S3). In all the cases, the solution nonideality dominates the Li diffusion kinetics. At a mild charging condition (1C), the stress potential adds more heterogeneity in Li distribution within the polycrystalline particle. However, its effect appears more negligible at a higher charging rate (10C) (Supplementary Fig. S4). Therefore, we conclude that the thermodynamic nonideality in the concentrated solution predominantly determines the voltage response, capacity, and Li distribution in the NMC polycrystalline particle at the galvanostatic charging condition.

### 3.3. Electrolyte infiltration and its impact on electrochemistry and mechanics

We use the 2D half-cell model and apply the coupled chemomechanics-damage theory outlined in Sections 2.1, 2.2 and 3.1.

We use the cohesive zone model to simulate fracture initiation and growth dynamics. The half cell is charged and discharged at a 1C charging rate, and the computational results in the following two subsections are presented at the end of the first charging. Significant intergranular fracture is observed upon the first cycle that is consistent with previous experimental results [4]. In this section, we address three aspects related to electrolyte infiltration along the mechanically damaged grain boundaries. First, we evaluate how the corrosion and redistribution of charge transfer kinetics at the freshly exposed surfaces modulate Li diffusion kinetics, electrochemical and mechanical behaviors. Second, we compare the effects of electrolyte infiltration on Li diffusion, mechanical response, and surface kinetics in the liquid versus solid-state electrolyte batteries. Electrolyte penetration along the grain network associated with mechanical damage is primarily a feature in liquid-electrolyte based cells, while solid-state batteries do not present such convolution. Lastly, we explore how the electrochemical response and mechanical behaviors of solid-state and liquid electrolyte batteries evolve over cycles, and how the coupling between mechanical damage and electrolyte infiltration propagates after the first galvanostatic charging cycle. Albeit limited by the computational cost of extensive cycles, modeling battery behaviors in the first few cycles regulated by the intimate coupling between electrochemistry and mechanical damage can shed insight in understanding the capacity retention and cyclic efficiency in the long-term usage.

### 3.3.1. Redistribution of charge transfer kinetics by liquid penetration and the corrosion effect

We evaluate the effects of corrosion and electrolyte penetration independently on Li distribution and mechanical damage within the cathode particle. We adopt a control group as a reference that does not consider corrosion or electrolyte infiltration along the fractured grain boundaries. In the following presentation referring to the corrosion effect, we assume that the fracture strength and fracture energy of the wetted surfaces by the electrolyte are half of those of pristine values. The considered underlying mechanisms are described in Section 2.4. The results referring to the penetration effect, on the other hand, incorporate redistribution of interfacial charge transfer kinetics on the freshly exposed surfaces.

Fig. 5(a)–(c) show the normalized Li concentration and intergranular fracture produced by the control group, and models considering the corrosion and penetration effects, respectively, at the end of the first charging. The white lines inside the polycrystalline particle represent the grain boundaries between the primary particles, while the black lines depict the fractured boundaries with the damage function being equal to one. Cracks are observed throughout the secondary particle in all the three cases and residual Li is trapped at the center. As discussed earlier, the corrosion effect is based on the consideration that the side reaction between the electrolyte and newly exposed surfaces erodes and weakens the mechanical cohesion between the primary particles, thus the NMC particle experiences a greater deal of mechanical damage upon charging (Fig. 5(a) and (b)). Fig. 5(d) shows the statistical average of mechanical damage of the cohesive elements within the particle during the first charging. The damage degree is much higher in the corrosion model compared to the control group throughout the charging process. The significant damage results in more residual Li at the center and thus less deliverable charging capacity because of the distorted pathway of Li transport through the damaged grain boundaries. Fig. 5(e) shows that the voltage profiles where the two models nearly overlap, demonstrating that the voltage response of the NMC cathode is predominately determined by the charge transfer kinetics at the particle surface and the corrosion effect has a limited impact on the surface event in the galvanostatic charging process. In comparison, in the model with the penetration effect (Fig. 5(c)), a much more uniform distribution of Li across the particle is observed compared to the control model. In this case, we consider that liquid electrolyte can easily access the freshly exposed grain boundaries due to the capillary motion (Supplementary Fig. S1),

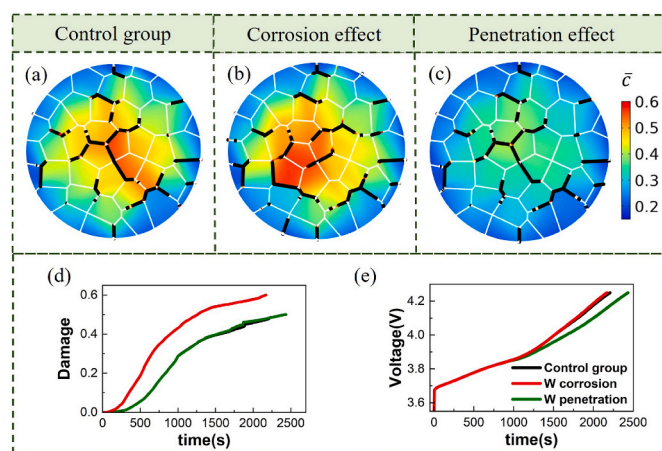


Fig. 5. Demonstration of the effects of corrosion and penetration of electrolyte infiltration along the grain boundaries on Li distribution and mechanical damage in the NMC secondary particle. (a)–(c) show the Li concentration and intergranular fracture at the end of the first charging in the control group (a) as a reference, by considering the corrosion effect (b), and by considering the penetration effect (c). The contour plots represent Li distribution, the white lines show the original grain boundaries between the primary particles, and the black lines represent intergranular fracture. (d) and (e) show the evolution of the average intergranular damage and the voltage profiles in the three sets of models during the first charging.

facilitating Li extraction from the center to the particle surface. The crack pattern compared to the control group looks similar. In the plot of the average mechanical damage in Fig. 5(d), the two models show largely overlapped profiles where the black curve represents the control group and the green line on the top shows the penetration model. Additionally, in the voltage response in Fig. 5(e), the cell takes longer time to reach the cutoff voltage with the presence of electrolyte penetration along the grain boundaries. This is consistent with the more uniform distribution of Li (and less trapped at the particle center) in the galvanostatic charging, resulting in a higher deliverable capacity of the cathode.

### 3.3.2. Solid-state and liquid electrolyte batteries

To further demonstrate the role of electrolyte infiltration in the electrochemical and mechanical behaviors of batteries, we build intact, solid-state, and liquid electrolyte models to compare their Li diffusion, mechanical response, and surface reaction kinetics in these battery systems. The intact model simulates the half cell without considering mechanical damage or electrolyte infiltration. For the solid-state battery model, we account for the presence of grain damage but not the corrosion or penetration effect since the solid-state electrolyte cannot infiltrate the cracks. In the liquid electrolyte model, we incorporate both damage and electrolyte infiltration, encompassing the corrosion effect and penetration along the grain boundaries.

Fig. 6 illustrates the concentration profile and crack distribution within the NMC particle at the end of the first charging for (a) the intact model, (b) the solid-state electrolyte model, and (c) the liquid electrolyte model. First, we examine the impact of damage on Li diffusion kinetics. The solid-state electrolyte model exhibits more residual Li at the particle center compared to the intact model. The presence of cracks obstructs Li transport, resulting in slower Li kinetics and a greater degree of concentration heterogeneity within the particle. Next, we investigate the effect of electrolyte infiltration on Li diffusion and the mechanical behavior. In comparison to the solid-state electrolyte model, the liquid case experiences a more homogenous charge distribution, despite more severe damage to the particle. Electrolyte infiltration along the cracks creates new surfaces where interfacial charge transfer takes place, in addition to the outer surface of the particle. Consequently, less Li

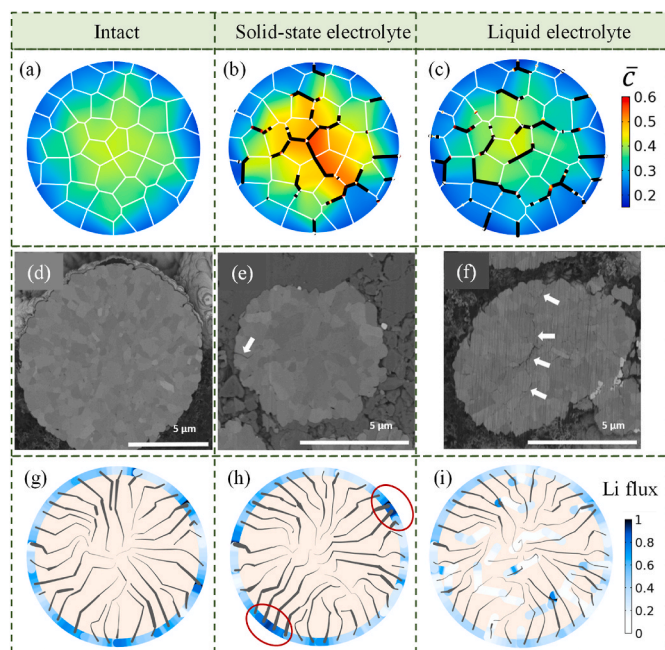


**Fig. 6.** Comparison of Li transport kinetics and mechanical damage of the NMC cathode in the intact configuration, with a solid-state electrolyte (no corrosion of the grain strength or electrolyte infiltration along the cracked surfaces), and with a liquid electrolyte (both corrosion and electrolyte infiltration in action) upon charging. (a)–(c) show Li distribution and the damage profile in the three models at the end of the first charging, respectively. Intergranular fracture clearly creates more heterogeneity of Li distribution, while corrosion and infiltration in the liquid electrolyte environment promote both Li transport and mechanical damage in the NMC particle. (d)–(f) show the SEM images of a pristine NMC secondary particle (d), intergranular fracture of NMC at the end of the first charging in a solid-state electrolyte environment (e) and with a liquid electrolyte (f). Arrows highlight the major cracks inside the NMC particles. Figures (d)–(f) are used with permission of IOP Publishing, Ltd [31]. (g)–(i) show the Li flux trajectory inside the particle and the flux magnitude at the outer and fractured surfaces in the three models, respectively. The red circles highlight the concentrated Li flux due to the mechanical damage regulated Li transport. (For interpretation of the references to color in this figure legend, the reader is referred to the Web version of this article.)

becomes trapped inside the particle, leading to a higher available capacity in the liquid electrolyte model. The simulation results and comparative behaviors are consistent with previous experimental observations [31], as shown in Fig. 6(d)–(f). Fig. 6(d) displays the cross-sectional SEM image of a pristine NMC particle, while Fig. 6(e) and (f) depict SEM images of NMC particles at the end of the first charging in all-solid-state and liquid electrolyte batteries, respectively. More mechanical cracking (highlighted by the white arrows) is observed in the NMC particles with the liquid electrolyte environment compared to the solid-state case. Additionally, the first-cycle voltage profile from the same experimental study showed a higher specific capacity in the liquid electrolyte batteries than in the solid-state counterpart. The consistent observations in both the mechanical and electrochemical performances validate our numerical modeling. In conclusion, liquid electrolyte infiltration improves Li diffusion kinetics and overall capacity, despite at the expense of a higher degree of mechanical damage. In a further analysis, we plot the trajectory of Li flux inside the NMC particle and the magnitude of charge transfer at the interface between the electrolyte and the active particle. Fig. 6(g)–(i) depict the Li flux pathways (grey streamlines) inside the particle and the Li flux magnitude (blue line) at the original and the fractured surfaces. The direction of Li flux aligns tangentially with the streamlines, and the width of the streamlines corresponds to the flux magnitude. Compared to the intact model, the solid-state electrolyte model exhibits highly concentrated spots for

charge transfer at the outer surfaces. With the formation and growth of cracks, certain Li channels inside the particle are blocked, resulting in more distorted and crowded pathways of Li transport at the outer surface (highlighted by the red circles in Fig. 6(e)). The liquid electrolyte model displays the most uniform charge transfer distribution at the surface. Due to electrolyte infiltration at the fractured surface, Li near the center of the particle can rapidly access the electrolyte, bypassing the need to travel through the bulk to reach the outer surface (as in the intact and solid-state electrolyte models). Consequently, the NMC cathode in the liquid environment possesses an enhanced surface reaction area and effectively a reduced particle size. Although cracks block Li transport and undermine the electrochemistry performance, electrolyte infiltration partially compensates for the electrochemical degradation.

We would like to note that the numerical modeling considers electrolyte infiltration as long as intergranular fracture initiates at the grain boundaries. Nevertheless, certain damage, particularly residing near the center of the particle, may not have immediate access to the electrolyte. This is represented by the minor crack depicted in the schematic of Fig. 1 (a) and observed in previous experiments [35,43,47,48]. Hence, it would be more accurate to consider the accessibility of electrolyte infiltration of the grain boundaries by evaluating their connectivity with the neighboring grains and pathway toward the outer surface. The numerical calibration on the electrolyte accessibility is presented in the Supplementary Fig. S5, and the detailed procedure is described in the supplementary note. We note that while the inclusion of the electrolyte accessibility increases the computational cost during the dynamic growth of mechanical damage, the qualitative results of the damage profile and Li distribution within the NMC particle remain unchanged.

### 3.3.3. Co-evolved electrochemical response and mechanical damage over cycles

Moving forward from the assessment on the initial charging behavior, we investigate the co-evolved electrochemical performance and mechanical damage over the first few cycles. It should be noted that the numerical modeling is not intended to replicate the long-term cycling behavior of batteries in experiments, which is computationally expensive, but is to provide qualitative understanding on the time evolution of the considered multiphysics associated with the charging and discharging cycles. Fig. 7(a) and (b) show the Li distribution and damage profile within the NMC polycrystalline particle with a solid-state and a liquid electrolyte at the end of the first three charging processes. In both models, the patterns of Li distribution and intergranular fracture remain nearly unchanged after the first charging is completed, indicating that major mechanical damage occurs during the first charging process, and the cell behavior becomes stable in the following cycles. The emergence of major structural disintegration of NMC cathode particles in the first cycle is consistent with the previous experimental reports [4,42]. Fig. 7(c), (d), and (e) demonstrate the impact of electrolyte infiltration on the evolution of voltage response, capacity retention, and average damage over three charge-discharge cycles. The capacity ratio is calculated by dividing the charge capacity in each cycle by the first charge capacity of the intact model (without fracture). The capacity ratio and average damage of the grain network are shown in Fig. 7(d) and (e), respectively. The capacity difference between the first and the following cycles arises from the limitation of Li diffusivity at the given charging rate. Mechanical damage in the solid-state electrolyte hinders Li diffusion, resulting in the partial capacity loss compared to the intact model. In comparison, infiltration of the liquid electrolyte improves Li diffusion kinetics by providing additional locations for interfacial charge transfer to take place, thus compensating for the reduction of capacity loss caused by fracture. The liquid electrolyte cell exhibits a similar capacity to the intact model. Among the three models, the cell capacity ratio remains constant after the first cycle since mechanical damage is saturated and no new fracture grows along the grain boundaries in the subsequent cycles.

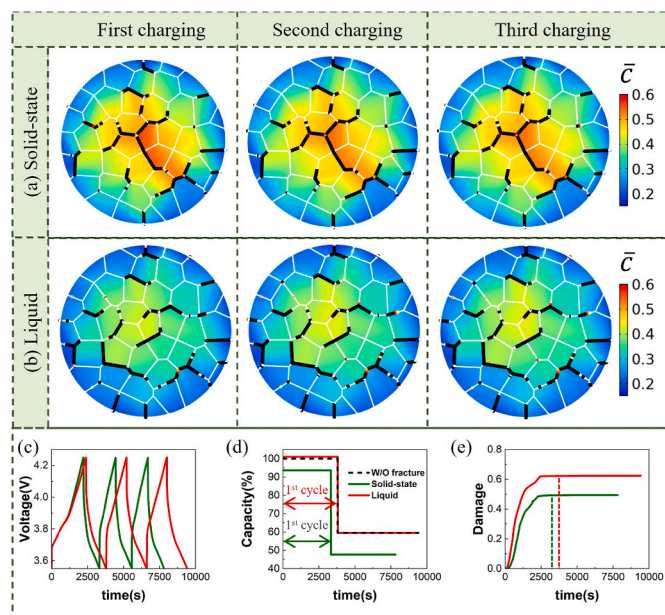


**Fig. 7.** Demonstration of the effect of electrolyte infiltration on co-evolved electrochemical responses and mechanical damage of NMC cathode over the first few cycles. (a)–(b) show the Li concentration and the damage profile in NMC with a solid-state electrolyte (without electrolyte infiltration) and a liquid electrolyte (with infiltration effect) at the end of the first three charging at 1C. (c)–(e) show the comparison of the voltage responses, capacity retention, and the average damage parameter in the solid-state and liquid environments, respectively. The dashed black line in (d) displays the capacity for the intact model as a reference, where the capacity drop is due to the limited Li diffusivity. The mechanical damage in the solid environment deteriorates the accessible capacity of NMC, while electrolyte infiltration in the liquid environment compensates for the adverse effect of the mechanical damage. The dashed lines in (e) indicate the end of the first cycle. It shows that mechanical damage is primarily generated in the first cycle at this charging rate and remains steady in the later cycles.

#### 4. Conclusions

In summary, we present a computational framework that integrates electrochemistry and mechanical damage of a ternary layered oxide composite cathode for Li-ion batteries. The theory incorporates thermodynamic nonideality of a concentrated solution, anisotropic Li diffusivity, concentration-dependent and anisotropic mechanical properties, and anisotropic chemical strains. The results from the finite element analysis reveal the concurrent crack growth and electrolyte infiltration along the grain boundaries, and their impact on Li kinetics and damage evolution within the NMC polycrystalline particle and voltage response and capacity retention of the cell. Anisotropy plays a key role where the anisotropic strain results in highly concentrated stresses at the grain boundaries and major structural decohesion upon the first charging, and the anisotropic transport and mechanical properties give rise to tortuous Li diffusion pathways within the active particle and lead to heterogeneous concentration and stress distributions. In the mechanics-transport coupling, the stress potential and the change of material stiffness at different SOCs do not significantly alter the Li diffusion kinetics in the NMC polycrystalline particle; the solution nonideality plays the major role in regulating Li flux especially at high charging rates. We consider that intergranular fracture is not merely a mechanical cleavage process, but also is accompanied by electrolyte infiltration along the damaged grain boundaries by capillary motion. The exposure of freshly cracked surfaces to the electrolyte provides additional sites for interfacial charge transfer in the interior regions of the active particle, effectively reducing the particle size and increasing the deliverable capacity at a given charging rate. Nevertheless,

electrolyte infiltration also corrodes the surface of the primary particles and weakens the mechanical strength of the polycrystalline particle which aggravates further mechanical damage. The effect of electrolyte penetration is demonstrated in the comparative behaviors of cells with a solid-state electrolyte and a liquid electrolyte. Electrolyte infiltration improves Li diffusion kinetics and overall capacity of the cell albeit at the expense of a higher degree of mechanical degradation. We observe that most particle damage takes place during the first charging of NMC in both solid-state and liquid electrolytes. Over the first few cycles, both the electrochemical response and structural disintegration remain steady after the completion of the first charging. The nonlinear damage growth is consistent with experimental observations. Overall, we highlight the dynamic nature between the electrochemical kinetics, including Li transport and surface charge transfer, and mechanical damage within the grain network. The coevolution of electrochemistry and mechanical failure features the complex mechanism of battery degradation in commercial use.

#### 5. Methods

We implement finite element analysis to solve the coupled electrochemistry-damage equations outlined in Section 2 for the composite cathode upon galvanostatic charging/discharging. The weak formulations can be found in a previous work [14]. The multiphysics time-dependent solver MUMPS (MULTifrontal MASSively Parallel sparse direct Solver) in COMSOL is used to solve the co-evolution of the Li diffusion kinetics, electron transport kinetics, mechanical stresses and damage. The test function for the electrolyte potential, electrolyte salt concentration, and electric potential is quadratic and the order and shape of the test functions for the chemical potential and displacement are quadratic Lagrange.

#### Disclaimer

This report was prepared as an account of work sponsored by an agency of the United States Government. Neither the United States Government nor any agency thereof, nor any of their employees, makes any warranty, express or implied, or assumes any legal liability or responsibility for the accuracy, completeness, or usefulness of any information, apparatus, product, or process disclosed, or represents that its use would not infringe privately owned rights. Reference herein to any specific commercial product, process, or service by trade name, trademark, manufacturer, or otherwise does not necessarily constitute or imply its endorsement, recommendation, or favoring by the United States Government or any agency thereof. The views and opinions of authors expressed herein do not necessarily state or reflect those of the United States Government or any agency thereof.

#### CRediT authorship contribution statement

**Jiaxiu Han:** Writing – review & editing, Writing – original draft, Methodology, Investigation, Formal analysis, Data curation. **Nikhil Sharma:** Writing – review & editing, Writing – original draft, Methodology, Investigation, Formal analysis, Data curation. **Kejie Zhao:** Writing – review & editing, Writing – original draft, Supervision, Project administration, Methodology, Investigation, Funding acquisition, Data curation, Conceptualization.

#### Declaration of competing interest

The authors declare that they have no known competing financial interests or personal relationships that could have appeared to influence the work reported in this paper.

## Data availability

Data will be made available on request.

## Acknowledgment

This material is based upon work supported by the U.S. Department of Energy, Office of Science, Office of Basic Energy Sciences, under Award Number DE-SC0024064. The authors are grateful for the discussions with Prof. Qian Chen and Prof. Jian-Min Zuo at University of Illinois Urbana-Champaign.

## Appendix A. Supplementary data

Supplementary data to this article can be found online at <https://doi.org/10.1016/j.jpowsour.2023.234034>.

## References

- [1] International Energy Agency, Net Zero by 2050 – A Roadmap for the Global Energy Sector, 2021.
- [2] Y. Ding, Z.P. Cano, A. Yu, J. Lu, Z. Chen, Automotive Li-ion batteries: current status and future perspectives, *Electrochem. Energy Rev.* 2 (2019) 1–28, <https://doi.org/10.1007/S41918-018-0022-Z>.
- [3] N. Nitta, F. Wu, J.T. Lee, G. Yushin, Li-ion battery materials: present and future, *Mater. Today* 18 (2015) 252–264, <https://doi.org/10.1016/J.MATOD.2014.10.040>.
- [4] H.H. Ryu, K.J. Park, C.S. Yoon, Y.K. Sun, Capacity fading of Ni-rich Li[Ni<sub>x</sub>Co<sub>y</sub>Mn<sub>1-x-y</sub>O<sub>2</sub>] (0.6 ≤ x ≤ 0.95) cathodes for high-energy-density Lithium-ion batteries: bulk or surface degradation? *Chem. Mater.* 30 (2018) 1155–1163, <https://doi.org/10.1021/ACS.CHEMMATER.7B05269>.
- [5] L.S. De Vasconcelos, R. Xu, Z. Xu, J. Zhang, N. Sharma, S.R. Shah, J. Han, X. He, X. Wu, H. Sun, S. Hu, M. Perrin, X. Wang, Y. Liu, F. Lin, Y. Cui, K. Zhao, Chemomechanics of rechargeable batteries: status, theories, and perspectives, *Chem. Rev.* 122 (2022) 13043–13107, <https://doi.org/10.1021/acs.chemrev.2c00002>.
- [6] Z. Xu, Z. Jiang, C. Kuai, R. Xu, C. Qin, Y. Zhang, M.M. Rahman, C. Wei, D. Nordlund, C.J. Sun, X. Xiao, X.W. Du, K. Zhao, P. Yan, Y. Liu, F. Lin, Charge distribution guided by grain crystallographic orientations in polycrystalline battery materials, *Nat. Commun.* 11 (2020) 83, <https://doi.org/10.1038/s41467-019-13884-x>.
- [7] N. Sharma, D. Meng, X. Wu, L.S. de Vasconcelos, L. Li, K. Zhao, Nanoindentation measurements of anisotropic mechanical properties of single crystalline NMC cathodes for Li-ion batteries, *Extreme Mech. Lett.* 58 (2023) 101920, <https://doi.org/10.1016/J.EML.2022.101920>.
- [8] K. Märker, P.J. Reeves, C. Xu, K.J. Griffith, C.P. Grey, Evolution of structure and Lithium dynamics in LiNi<sub>0.8</sub>Mn<sub>0.1</sub>Co<sub>0.1</sub>O<sub>2</sub> (NMC811) cathodes during electrochemical cycling, *Chem. Mater.* 31 (2019) 2545–2554, <https://doi.org/10.1021/ACS.CHEMMATER.9B00140>.
- [9] A. van Bommel, J.R. Dahn, Synthesis of spherical and dense particles of the pure hydroxide phase Ni<sub>1/3</sub>Mn<sub>1/3</sub>Co<sub>1/3</sub>(OH)<sub>2</sub>, *J. Electrochem. Soc.* 156 (2009), <https://doi.org/10.1149/1.3079366>, A362–A365.
- [10] X. Wu, B. Song, P.-H. Chien, S.M. Everett, K. Zhao, J. Liu, Z. Du, X. Wu, Z. Du, K. Zhao, B. Song, P.-H. Chien, S.M. Everett, J. Liu, Structural evolution and transition dynamics in Lithium ion battery under fast charging: an operando neutron diffraction investigation, *Adv. Sci.* 8 (2021) 2102318, <https://doi.org/10.1002/ADVS.202102318>.
- [11] A.O. Kondrakov, A. Schmidt, J. Xu, H. Geßwein, R. Mönig, P. Hartmann, H. Sommer, T. Brezesinski, J. Janek, Anisotropic lattice strain and mechanical degradation of high- and low-Nickel NCM cathode materials for Li-ion batteries, *J. Phys. Chem. C* 121 (2017) 3286–3294, <https://doi.org/10.1021/acs.jpcc.6b12885>.
- [12] P. Liu, R. Xu, Y. Liu, F. Lin, K. Zhao, Computational modeling of heterogeneity of stress, charge, and cyclic damage in composite electrodes of Li-ion batteries, *J. Electrochem. Soc.* 167 (2020) 040527, <https://doi.org/10.1149/1945-7111/ab78fa>.
- [13] S.R. Shah, L.S. De Vasconcelos, K. Zhao, Computational modeling of electrochemomechanics of high-capacity composite electrodes in Li-ion batteries, *J. Appl. Mech.* 89 (2022) 081005, <https://doi.org/10.1115/1.4054759>.
- [14] R. Xu, L. Scalco De Vasconcelos, K. Zhao, Computational analysis of chemomechanical behaviors of composite electrodes in Li-ion batteries, *J. Mater. Res.* 31 (2016) 2715–2727, <https://doi.org/10.1557/jmr.2016.302>.
- [15] R. Xu, K. Zhao, Mechanical interactions regulated kinetics and morphology of composite electrodes in Li-ion batteries, *Extreme Mech. Lett.* 8 (2016) 13–21, <https://doi.org/10.1016/j.eml.2015.10.004>.
- [16] M.W. Verbrugge, Modeling Lithium intercalation of single-fiber carbon microelectrodes, *J. Electrochem. Soc.* 143 (1996) 600, <https://doi.org/10.1149/1.1836486>.
- [17] G. Bucci, S.P.V. Nadimpalli, V.A. Sethuraman, A.F. Bower, P.R. Guduru, Measurement and modeling of the mechanical and electrochemical response of amorphous Si thin film electrodes during cyclic lithiation, *J. Mech. Phys. Solid.* 62 (2014) 276–294, <https://doi.org/10.1016/j.jmps.2013.10.005>.
- [18] L.S. de Vasconcelos, R. Xu, K. Zhao, Quantitative spatiotemporal Li profiling using nanoindentation, *J. Mech. Phys. Solid.* 144 (2020) 104102, <https://doi.org/10.1016/j.jmps.2020.104102>.
- [19] S. Yin, W. Deng, J. Chen, X. Gao, G. Zou, H. Hou, X. Ji, Fundamental and solutions of microcrack in Ni-rich layered oxide cathode materials of lithium-ion batteries, *Nano Energy* 83 (2021) 105854, <https://doi.org/10.1016/J.NANOEN.2021.105854>.
- [20] H. Liu, M. Wolf, K. Karki, Y.S. Yu, E.A. Stach, J. Cabana, K.W. Chapman, P. J. Chupas, Intergranular cracking as a major cause of long-term capacity fading of layered cathodes, *Nano Lett.* 17 (2017) 3452–3457, <https://doi.org/10.1021/acs.nanolett.7b00379>.
- [21] H. Tian, L.T. Gao, Z.-S. Guo, Microstructural adjusting crack evolution of polycrystalline NCM particle during charge/discharge cycle, *J. Electrochem. Soc.* 169 (2022) 090513, <https://doi.org/10.1149/1945-7111/ac8ee3>.
- [22] K. Taghikhani, P.J. Weddle, J.R. Berger, R.J. Kee, Modeling coupled chemo-mechanical behavior of randomly oriented NMC811 polycrystalline Li-ion battery cathodes, *J. Electrochem. Soc.* 168 (2021) 080511, <https://doi.org/10.1149/1945-7111/ac1811>.
- [23] K. Taghikhani, P.J. Weddle, R.M. Hoffman, J.R. Berger, R.J. Kee, Electro-chemo-mechanical finite-element model of single-crystal and polycrystalline NMC cathode particles embedded in an argyrodite solid electrolyte, *Electrochim. Acta* 460 (2023) 142585, <https://doi.org/10.1016/j.electacta.2023.142585>.
- [24] J.M. Allen, P.J. Weddle, A. Verma, A. Mallarapu, F. Ueseglio-Viretta, D.P. Finegan, A.M. Colclasure, W. Mai, V. Schmidt, O. Furat, D. Diercks, T. Tanim, K. Smith, Quantifying the influence of charge rate and cathode-particle architectures on degradation of Li-ion cells through 3D continuum-level damage models, *J. Power Sources* 512 (2021) 230415, <https://doi.org/10.1016/j.jpowsour.2021.230415>.
- [25] A. Singh, S. Pal, Chemo-mechanical modeling of inter- and intra-granular fracture in heterogeneous cathode with polycrystalline particles for lithium-ion battery, *J. Mech. Phys. Solid.* 163 (2022) 104839, <https://doi.org/10.1016/j.jmps.2022.104839>.
- [26] F. Lin, I.M. Markus, D. Nordlund, T.C. Weng, M.D. Asta, H.L. Xin, M.M. Doeff, Surface reconstruction and chemical evolution of stoichiometric layered cathode materials for lithium-ion batteries, *Nat. Commun.* 5 (2014) 3529, <https://doi.org/10.1038/ncomms4529>.
- [27] L. Mu, R. Lin, R. Xu, L. Han, S. Xia, D. Sokaras, J.D. Steiner, T.C. Weng, D. Nordlund, M.M. Doeff, Y. Liu, K. Zhao, H.L. Xin, F. Lin, Oxygen release induced chemomechanical breakdown of layered cathode materials, *Nano Lett.* 18 (2018) 3241–3249, <https://doi.org/10.1021/acs.nanolett.8b01036>.
- [28] G. Qian, G. Zan, J. Li, J. Zhang, P. Pianetta, Y. Liu, In-situ visualization of the transition metal dissolution in layered cathodes, *J. Electrochem. Energy Convers. Storage* 19 (2022) 041002, <https://doi.org/10.1115/1.4054584>.
- [29] X. Liu, X. Zhan, Z.D. Hood, W. Li, D.N. Leonard, A. Manthiram, M. Chi, Essential effect of the electrolyte on the mechanical and chemical degradation of LiNi<sub>0.8</sub>Co<sub>0.15</sub>Al<sub>0.05</sub>O<sub>2</sub> cathodes upon long-term cycling, *J. Mater. Chem. A Mater.* 9 (2021) 2111–2119, <https://doi.org/10.1039/D0TA07814J>.
- [30] S. Xia, L. Mu, Z. Xu, J. Wang, C. Wei, L. Liu, P. Pianetta, K. Zhao, X. Yu, F. Lin, Y. Liu, Chemomechanical interplay of layered cathode materials undergoing fast charging in lithium batteries, *Nano Energy* 53 (2018) 753–762, <https://doi.org/10.1016/j.nanoen.2018.09.051>.
- [31] R. Ruess, S. Schweidler, H. Hemmelmann, G. Conforto, A. Bielefeld, D.A. Weber, J. Sann, M.T.T. Elm, J. Janek, Influence of NCM particle cracking on kinetics of Lithium-ion batteries with liquid or solid electrolyte, *J. Electrochem. Soc.* 167 (2020) 100532, <https://doi.org/10.1149/1945-7111/ab9a2c>.
- [32] J. Min, L.M. Gubow, R.J. Hargrave, J.B. Siegel, Y. Li, Direct measurements of size-independent lithium diffusion and reaction times in individual polycrystalline battery particles, *Energy Environ. Sci.* 16 (2023) 3847, <https://doi.org/10.1039/d3ee00953j>.
- [33] S. Li, Z. Jiang, J. Han, Z. Xu, C. Wang, H. Huang, C. Yu, S.J. Lee, P. Pianetta, H. Ohldag, J. Qiu, J.S. Lee, F. Lin, K. Zhao, Y. Liu, Mutual modulation between surface chemistry and bulk microstructure within secondary particles of nickel-rich layered oxides, *Nat. Commun.* 11 (2020) 4433, <https://doi.org/10.1038/s41467-020-18278-y>.
- [34] R. Xu, L.S. de Vasconcelos, J. Shi, J. Li, K. Zhao, Disintegration of meatball electrodes for LiNi<sub>x</sub>Mn<sub>y</sub>Co<sub>z</sub>O<sub>2</sub> cathode materials, *Exp. Mech.* 58 (2018) 549–559, <https://doi.org/10.1007/s11340-017-0292-0>.
- [35] D.J. Miller, C. Proff, J.G. Wen, D.P. Abraham, J. Bareño, Observation of microstructural evolution in li battery cathode oxide particles by in situ electron microscopy, *Adv. Energy Mater.* 3 (2013) 1098–1103, <https://doi.org/10.1002/aenm.201300015>.
- [36] F. Larché, J.W. Cahn, A linear theory of thermochemical equilibrium of solids under stress, *Acta Metall.* 21 (1973) 1051–1063, [https://doi.org/10.1016/0001-6160\(73\)90021-7](https://doi.org/10.1016/0001-6160(73)90021-7).
- [37] X. He, R. Xu, X. Ding, Anisotropic Mechanical Properties of Li[Ni<sub>x</sub>Mn<sub>y</sub>Co<sub>1-x-y</sub>O<sub>2</sub>] Cathodes for Li-Ion Batteries: A First-Principles Theoretical Study, submitted for publication.
- [38] M.S. Wu, T.L. Liao, Y.Y. Wang, C.C. Wan, Assessment of the wettability of porous electrodes for Lithium-ion batteries, *J. Appl. Electrochem.* 34 (2004) 797–805, <https://doi.org/10.1023/B:JACH.0000035599.56679.15>.
- [39] A. Davoodabadi, J. Li, Y. Liang, D.L. Wood, T.J. Singler, C. Jin, Analysis of electrolyte imbibition through lithium-ion battery electrodes, *J. Power Sources* 424 (2019) 193–203, <https://doi.org/10.1016/J.JPOWSOUR.2019.03.115>.

- [40] M. Doyle, T.F. Fuller, J. Newman, Modeling of galvanostatic charge and discharge of the Lithium/polymer/insertion cell, *J. Electrochem. Soc.* 140 (1993) 1526–1533, <https://doi.org/10.1149/1.2221597/XML>.
- [41] L.S. de Vasconcelos, N. Sharma, R. Xu, K. Zhao, In-Situ nanoindentation measurement of local mechanical behavior of a Li-ion battery cathode in liquid electrolyte, *Exp. Mech.* 59 (2019) 337–347, <https://doi.org/10.1007/s11340-018-00451-6>.
- [42] R. Xu, H. Sun, L. Scalco De Vasconcelos, K. Zhao, Mechanical and structural degradation of LiNi<sub>x</sub>Mn<sub>y</sub>Co<sub>z</sub>O<sub>2</sub> cathode in Li-ion batteries: an experimental study, *J. Electrochem. Soc.* 164 (2017) 3333–3341, <https://doi.org/10.1149/2.1751713jes>.
- [43] I. Li, W.M. Dose, C. Villa, X. Hu, Characterization of electronic and ionic transport in Li<sub>1-x</sub>Ni<sub>0.33</sub>Mn<sub>0.33</sub>Co<sub>0.33</sub>O<sub>2</sub> (NMC333) and Li<sub>1-x</sub>Ni<sub>0.50</sub>Mn<sub>0.20</sub>Co<sub>0.30</sub>O<sub>2</sub> (NMC523) as a function of Li content, *J. Electrochem. Soc.* 163 (2016), <https://doi.org/10.1149/2.0131608JES>. A1512–A1517.
- [44] R. Xu, K. Zhao, Corrosive fracture of electrodes in Li-ion batteries, *J. Mech. Phys. Solid.* 121 (2018) 258–280, <https://doi.org/10.1016/j.jmps.2018.07.021>.
- [45] N. Sharma, L.S. De Vasconcelos, S. Hassan, K. Zhao, Asynchronous-to-synchronous transition of Li reactions in solid-solution cathodes, *Nano Lett.* 22 (2022) 5883–5890, <https://doi.org/10.1021/ACS.NANOLETT.2C01818>.
- [46] V.V. Bannikov, I.R. Shein, A.L. Ivanovskii, Elastic and electronic properties of hexagonal rhenium sub-nitrides Re<sub>3</sub>N and Re<sub>2</sub>N in comparison with hcp-Re and wurtzite-like rhenium mononitride ReN, *Phys. Status Solidi B* 248 (2011) 1369–1374, <https://doi.org/10.1002/PSSB.201046564>.
- [47] S. Schweidler, L. De Biasi, G. Garcia, A. Mazilkin, P. Hartmann, T. Brezesinski, J. Janek, Investigation into mechanical degradation and fatigue of high-Ni NCM cathode material: a long-term cycling study of full cells, *ACS Appl. Energy Mater.* 2 (2019) 7375–7384, <https://doi.org/10.1021/acsam.9b01354>.
- [48] Y. Mao, X. Wang, S. Xia, K. Zhang, C. Wei, S. Bak, Z. Shadike, X. Liu, Y. Yang, R. Xu, P. Pianetta, S. Ermon, E. Stavitski, K. Zhao, Z. Xu, F. Lin, X.Q. Yang, E. Hu, Y. Liu, High-voltage charging-induced strain, heterogeneity, and micro-cracks in secondary particles of a nickel-rich layered cathode material, *Adv. Funct. Mater.* 29 (2019) 1900247, <https://doi.org/10.1002/adfm.201900247>.